Facility Modifications for High Power Hall thruster Testing

William J. Hurley*, Liam McCarthy†, Byron Darrow, Braden Oh*, Tate Gill‡ and Benjamin Jorns§
University of Michigan, Ann Arbor, MI, 48109, United States

Abstract

A systematic experimental and numerical analysis of Hall thruster-induced heating of the cryopumps in the Large Vacuum Test Facility at the University of Michigan is performed. The goal of this analysis is to determine the necessary facility modifications to allow for extended duration 100 kW Hall thruster testing. Data from an 18 kW thruster test with krypton is used to inform thermal models for response of the pumps in the facility. The results indicate that the dominant factor curtailing test operation is the heating of pumps downstream of the thruster due to ion impingement. It is shown that for these downstream surfaces, beam impingement can cause cold head heating in excess of 0.3 W per kW of thruster power. Furthermore, deposited material from facility back sputter onto shroud surfaces induces a change in emissivity and reduces their ability to absorb heat from the environment. At high power levels, the combination of these effects can cause the pumps to exceed the minimum temperatures necessary for cryopumping. Proposed mitigation strategies include a restoration of pump emissivity, movement of the thruster downstream to avoid impingement, and a large water cooled beam dump to extract beam power. Thermal simulations predict that with these changes the facility will be able to handle 100 kW Hall thruster testing while maintaining pump surface temperatures below the saturation limits of krypton gas.

1 Introduction

Electric propulsion devices in the 100-200 kW class will be essential to support crewed and cargo transfers in cislunar and interplanetary space. This is evidenced in large part by NASA's strategic road map for Mars transfers, which among other high-power electric propulsion devices, features arrays of ∼20, 100 kW xenon Hall thrusters [1, 2, 3]. Hall thrusters, which employ electric and magnetic fields to accelerate ions and produce thrust, are now the most widely flown electric propulsion device. The growing dominance of Hall thrusters in orbit is driven by their ideal combination of system efficiency, size, and complexity. These traits have also made Hall thrusters attractive candidates to scale from the 1-10 kW class to >100 kW.

*PhD Candidate, Aerospace Engineering, University of Michigan
†Masters Student, Aerospace Engineering, University of Michigan
‡Research Engineer, Aerospace Engineering, University of Michigan
§Associate Professor, Aerospace Engineering, University of Michigan

To date, despite the potential benefits of this system, there have been no Hall thrusters flown and very few ground tested at power levels >50 kW. To the authors' knowledge, the longest duration high power test is of the X3 nested channel Hall thruster at 73.5 kW for $\sim$ 8 hours in the VF5 chamber at NASA Glenn [4]. The lack of experience is largely driven by the difficulties in ground testing high powered Hall thrusters.

Most notably, the key testing challenge is being able accurately replicate the in space environment. Factors known as "facility effects", such as finite background pressure, grounded facility walls, and deposition of sputtered material are all elements that can change the way Hall thrusters operate compared to on orbit. These facility effects are exacerbated at higher thruster powers, making representative testing extremely challenging.

To achieve low background pressures ($< 1 \times 10^{-5}$ Torr) and high pumping speeds, state of the art electric propulsion test facilities utilize cryopumps at 15-40 K to rapidly condense and remove gas from the vacuum chamber. Maintaining cryopumps at low temperatures becomes increasingly difficult as the thruster power level increases. The challenge results from both enhanced radiative loads to the cryopumps surfaces and higher propellant condensation rates. As a notable example, pump heating was prominently observed during short duration testing of the H9 Hall thruster operating at the elevated power of 45 kW the University of Michigan's Alec D. Gallimore large vacuum test facility (LVTF) [5, 6]. During this test campaign, the authors found that the cryopump surfaces warmed rapidly, which precluded an attempted long duration test. Therefore, to perform duration tests in LVTF at high power, there is a pressing need to investigate the physical mechanisms driving cryopump heating.

To address this need, we aim to identify and mitigate the major drivers of pump heating at high powers in LVTF. To accomplish this, we first perform extended duration $>$ 3 hr testing in LVTF at 18 kW. Using facility thermocouple data and a thermal model, we identify the major drivers of pump heating. From this analysis, we design and implement key solutions to allow for longer duration high powered testing in LVTF.

2 Cryopump Operation and Heating Mechanisms

Fig. 1 shows an example of a typical LN_2 shrouded cryopump with the sources of heating during thruster operation. As shown here, a common cryopump design utilized in EP testing consists of a cold head (15-25 K) inside of a liquid nitrogen shroud. Liquid helium refrigeration cycles, comprised of a cryocooler and a compressor, provide the cold head cooling. The shroud is designed to reduce the radiative loading to the cold head, thus lowering the necessary cooling capacity of the cryocooler. The dominant heating mechanisms to the pump during testing consist of propellant energy, direct thruster beam impingement heating the shroud, and facility radiation.

2.1 Heating from propellant thermal energy

Propellant in the facility deposits power when it contacts cold pump surfaces. We can represent this energy as three distant modes:

$$P_{prop} = \dot{m}_{prop}(h_{dep} + c_p(T_{prop} - T_{pump}) + 1/2v_{bulk}^2) \tag{1}$$

where P_{prop} is the propellant heat load, $\dot{m}_{prop}$ is the propellant mass flow rate, h_{dep} is the enthalpy of deposition, c_p is the gas specific heat, T_{prop} is average propellant temperature,

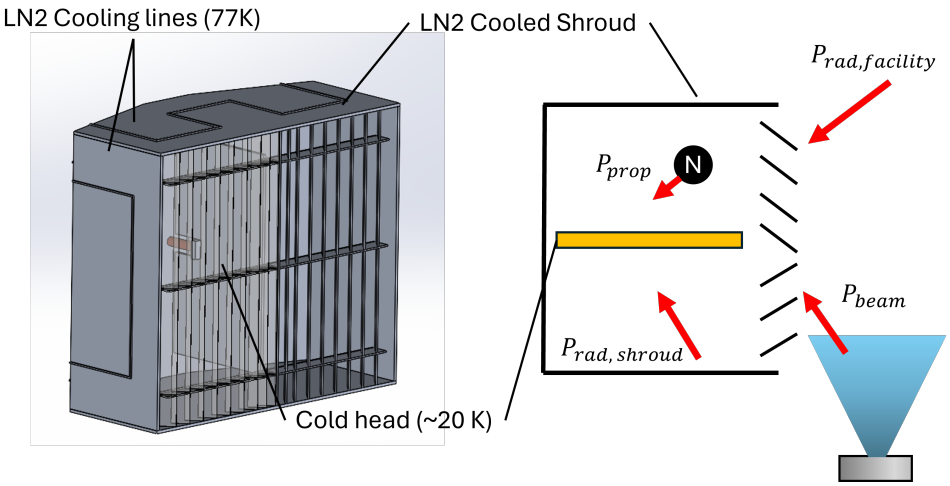

Figure 1: Example CAD geometry of a TM1200i shrouded cryopump and key pump heat sources.

T_{pump} is the cold head temperature, and v_{bulk} is the average directed velocity. Typical values for h_{dep} and c_p for xenon, krypton, argon, and nitrogen are taken from refs. [7, 8] and given in table 1. Also given is the approximate saturation temperature at 1×10^{-6} Torr for each propellant [9]. As an example, a 100 sccm flow rate of krypton that fully thermalizes with an 80 K LN_2 shroud ($T_{gas} = 80$ K, $v_{bulk} = 0$) provides 0.85 W of cold head heating.

Gas	h_{dep} (kJ/kg)	c_p (kJ/kg/K)	T_{sat} @1E-6 Torr (K)
Xenon	122.6	0.158	56
Krypton	137.3	0.248	41
Argon	202.8	0.520	28
Nitrogen	262	1.03 @ 300 K	25

Table 1: List of thermal properties for common EP propellants.

2.2 Heating from radiation and beam impingement

Both direct thruster beam impingement and facility radiation generally serve to heat the LN_2 shroud, which in turn radiates to the cold head. We note that any high velocity ions from direct beam impingement are captured by v_{bulk} in P_{prop}. Assuming the cold head is completely surrounded by the LN_2 shroud, the net radiative heat transfer between the shroud and the cold head is defined as

$$P_{rad,shroud} = \frac{\sigma(T_{shroud}^4 - T_{cold}^4)}{\frac{1-\epsilon_{cold}}{\epsilon_{cold}A_{cold}} + 1/A_{cold} + \frac{1-\epsilon_{shroud}}{\epsilon_{shroud}A_{shroud}}} \tag{2}$$

where σ is the Stephan-Boltzmann constant, ϵ is the total emissivity, T is the temperature, A is the surface area and the subscripts "cold" and "shroud" indicate the cold head and LN_2 shroud respectively [10]. Intuitively, eq. 2 demonstrates that as the shroud temperature or emissivity of either object decreases, the radiative heat transfer is lower. Assuming $T_{shroud} = 80$ K, $T_{cold} = 20$ K, $A_{shroud} \approx 1\ m^2$, $A_{cold} \approx 0.4\ m^2$, and the emissivities

are unity, $P_{rad,srhoud} = 0.93$ W. The effectiveness of a cold shroud is most evident when considering the thermal load with T_{shroud} at room temperature. In this case, the thermal loading to the cold head is more than two orders of magnitude higher at 183 W.

In isolation eq. 2 suggests that both the emissivity of the shroud and the cold head should be as low as possible to reduce cold head heating. While this strategy is effective if the only radiative loading to the cold head were from the shroud, facility radiation can reflect off the shroud surfaces and contact the cold head (fig. 2). Assuming the pump surfaces are opaque, the relationship between emissivity and reflectivity ρ is

$$1 = \epsilon + \rho. \tag{3}$$

As a result, LN_2 shroud surfaces are typically coated with a high emissivity material in order to completely absorb high temperature facility radiation. In sec. 4, we detail the 3D thermal modeling efforts for the cryopumps used in this test.

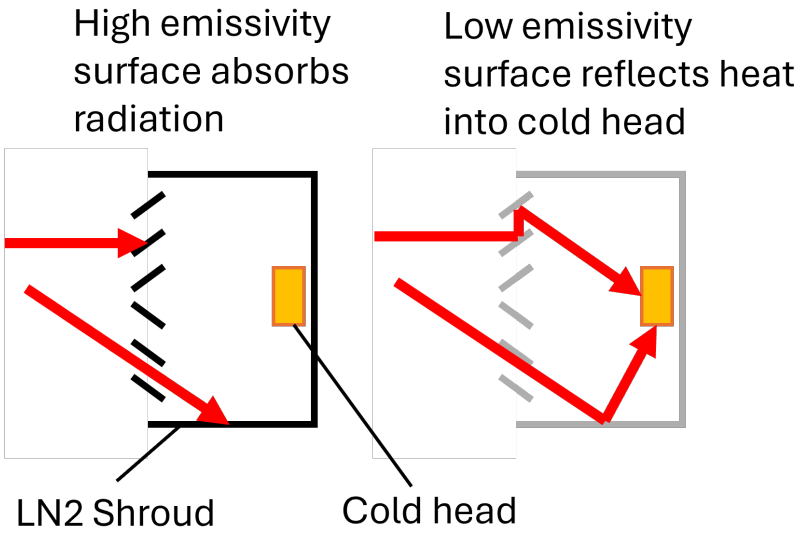

Figure 2: Facility radiation is absorbed or reflected by LN_2 shroud depending on emissivity.

3 Moderate Power Test Setup

Here, we overview the experimental campaign designed to measure pump thermal response to moderate power thruster testing. This includes cryopump specifications, design of a water cooled beam dump, and thruster operating conditions.

We operated a Hall thruster at 18 kW for an extended duration (> 3 hours) to help identify the major drivers of cryopump heating in LVTF. This data and the resulting analysis will inform what key changes are needed to perform duration testing at high powers (> 100 kW) in the test facility.

All testing was performed in the University of Michigan's Alec D. Gallimore Large Vacuum Test Facility [11]. This facility has 18 total cryopumps that line the chamber walls to rapidly condense propellant. 13 pumps are LN2 shrouded TM1200i's with a CRG 511 cryocooler. The CRG 511 cryocooler utilizes a two stage cooling scheme, with the first stage at 77 K, and the second at <20 K. The other 5 pumps are custom nude copper cryosails with an single stage AL600 Gifford-McMahon cryocooler [11]. In figure

3, we show the cooling capacity of the the CRG 511 cryocooler utilized for the TM1200i pumps as a function of first stage heating load P_1 [12]. As a first order approximation, we see that a cold head ΔT of 1 K corresponds to an additional 1 W of cooling.

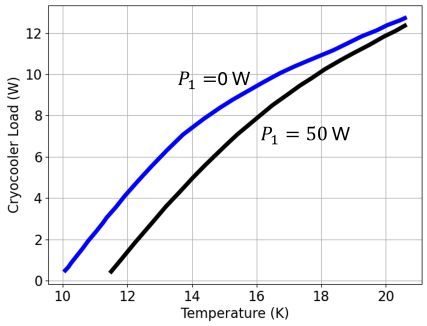

Figure 3: Performance of CRG 511 cryocooler with CBST 6.0 compressor as a function of first stage heat load (P_1). This data is reproduced from [12].

When fully operational the 18 pumps provide 600,000 L/s of pumping speed on krypton gas. For this work, we utilized 9 of the 13 shrouded pumps, and 2 of the 5 nude sails. All cryopumps have a silicon diode to monitor the cold head temperature [11]. Figure 4 illustrates the pump locations in LVTF, and which were operational for this campaign.

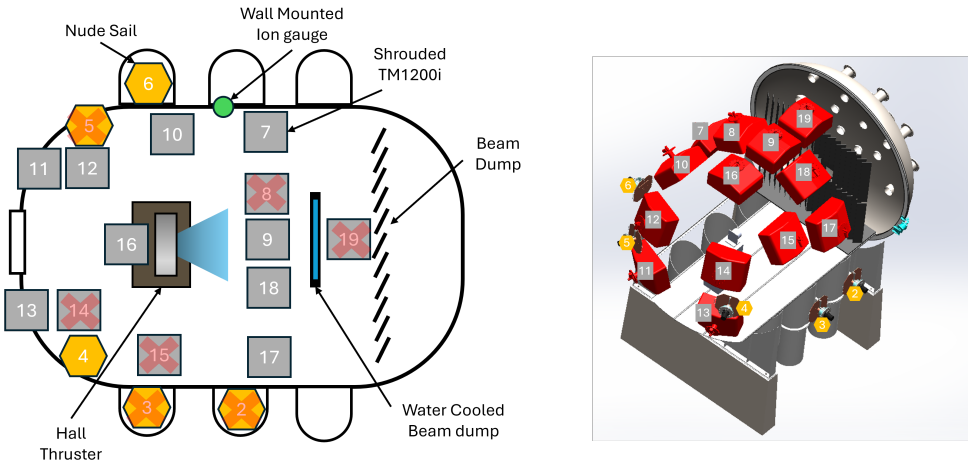

Figure 4: The experimental setup in LVTF for the moderate power test campaign. Included are the positions of the thruster, cryopumps, ion gauge, and beam dumps. The inactive cryopumps are denoted with a red "X".

To measure facility background pressure, we utilized a wall mounted IGM401 hot cathode ionization gauge. The gauge measures pressure in Torr-N2 with a listed accuracy of $\pm$ 15%. We correct the background pressure measurement from Torr-N2 to Torr-Kr by dividing by a factor of 1.94. This correction factor primarily accounts for the difference in ionization cross section between nitrogen and krypton. With the corrected pressure measurements and precisely controlled mass flow rate, we calculate the facility pumping speed as

$$S = \frac{\dot{m}}{P - P_{base}} \tag{4}$$

where S is the pumping speed, $\dot{m}$ is the mass flow rate, P is the ion gauge measured pressure, and P_{base} is the base pressure.

3.1 Prototype Water Cooled Beam Dump

One strategy to reduce thermal loading to pump surfaces is to use a water cooled beam dump to extract the thruster beam power. In principal, this will reduce the temperature of facility surfaces and thus the radiative load to the pumps. To assess the effectiveness of this strategy, we designed and implemented a small water cooled beam dump (WCBD). The design and setup of the WCBD in LVTF are shown in figure 5. The WCBD consists of two, 0.61 × 0.61 m graphite panels. We affix two 61 × 18 cm ATS tubed cold plates (ATS-TCP-1005) to each graphite panel. The water is parallelized to provide 1.5 gallons per minute (GPM) of flow to each of the four plates.

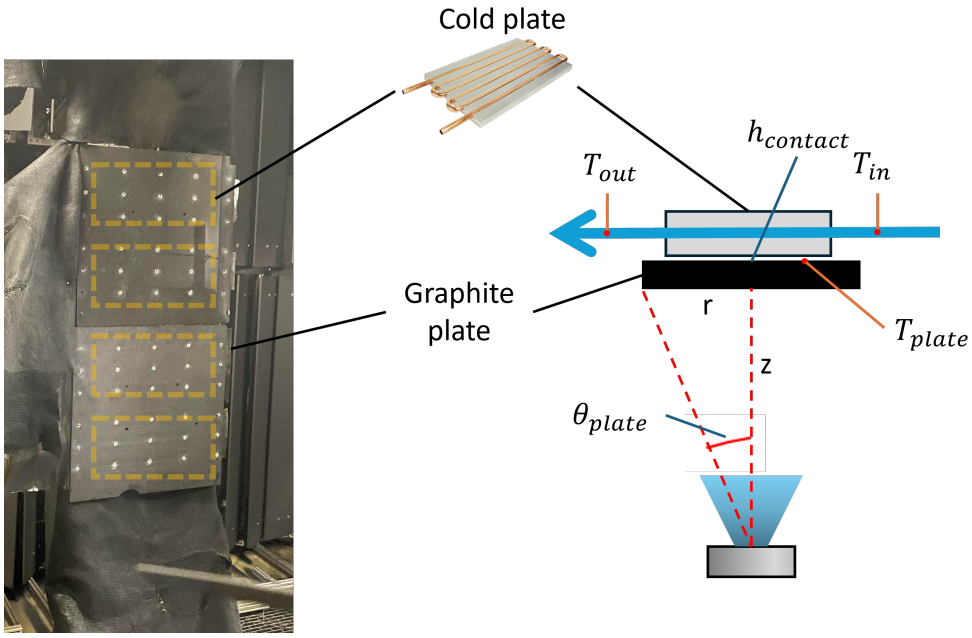

Figure 5: Small prototype water cooled beam dump installed in LVTF with a schematic of the geometry and temperature monitors.

When designing this WCBD, the two key considerations are the fraction of the beam power impacting the plate and the thermal impedance of heat from the graphite to the water. We discuss each facet in the following sections.

3.1.1 Beam power contacting WCBD

If we approximate the water cooled beam dump as a circle with radius r at a distance z from the thruster, we can estimate the fraction of beam power contacting the plate η_{plate} as

$$\eta_{plate} = \frac{\int_0^{tan^{-1}(z/r)} \alpha(\theta) I_b(\theta) V_a(\theta) d\theta}{\int_0^{\pi/2} I_b(\theta) V_a(\theta) d\theta} \tag{5}$$

where $I_b(\theta)$ and $V_a(\theta)$ are the azimuthal ion current and acceleration voltage distributions. $\alpha(\theta)$ is the accommodation coefficient as a function of incident angle. Physically, the accommodation coefficient represents the fraction of momentum transferred to the

graphite by an incident ion. For the purposes of this simple analysis, we assume perfect ion accommodation, $\alpha(\theta) = 1$. The acceleration voltage, $V_a(\theta)$, is a metric for ion kinetic energy and is typically measured with respect to the plasma potential.

This formulation implicitly assumes that the plume is azimuthally symmetric. We can estimate $I_b(\theta)$ with previously measured Faraday probe traces of the H9 operating on krypton at 15 kW [6]. While we do not have RPA measurements of the acceleration voltage with azimuthal angle for this effort, we assess two limiting cases to bound our estimate of η_{plate}. Most Hall thrusters typically exhibit a transition from primary main beam ions at high V_a in the center of the plume to a prominent low velocity scattered population at larger angles between 40-60° off centerline [13]. Since beam power scales with V_a, we expect the majority of the beam power to be concentrated in the center of the plume.

As a lower bound estimate, we assume V_a is constant across the plume and independent of θ. Evaluating eq. 5 with this scaling, we estimate that 23 % of the beam impacts the plate. As a potential upper bound estimate, we assume $V_a(\theta) \propto I_b(\theta)$ and revaluate eq. 5. This forms our upper bound estimate for η_{plate}= 55 %.

3.1.2 WCBD Thermal Impedance

The other key parameter of the WCBD is the thermal resistance to heat flow from the graphite plate to the water. Minimizing this resistance ensures that the graphite plate temperature and thus radiation to the pumps remains low. The total thermal resistance to heat flow is comprised of the contact resistance $h_{contact}$ from the graphite to the cold plate, and the resistance of heat from the cold plate to the water R_{water}. Per the manufacturer, R_{water} is 0.004 K/W for each cold plate. $h_{contact}$, which physically represents that the full area of the cold head is not in contact with the graphite, is hard to estimate in practice. The difficulty stems from the non-linear dependence of contact conductance on hard to estimate surface parameters like microhardness and pressure distributions [14]. As a result, we instead calibrate this parameter with the WCBD temperature measurements indicated in fig. 5 and a thermal model. We show in fig. 6 an example temperature distribution from the 3D COMSOL model of the WCBD.

In fig. 6, we apply a 6 kW heat load uniformly across the two graphite plates. We see the four discrete water cooled plate locations on the thermal model as indicated by the colder sections of the graphite plate. Ultimately, the effectiveness of the water cooled beam dump can be characterized as

$$\eta_{WCBD} = \frac{P_{water}}{P_{plate}} \tag{6}$$

where P_{water} is the power into the water and P_{plate} is the power to the graphite plates. We utilize the the water cooled beam dump thermal model in the larger facility simulations described in sec. 4.

3.2 Hall Thruster and Operating Conditions

For this effort, we utilized the H9 magnetically shielded Hall thruster [15]. The H9 was jointly developed by NASA JPL, the University of Michigan, and AFRL to serve as common test article for investigating thruster physics. The thruster employs a centrally mounted LaB_6 cathode to source electrons for the discharge. To understand the thermal response of the facility, we performed an extended duration test at 18 kW. The thruster

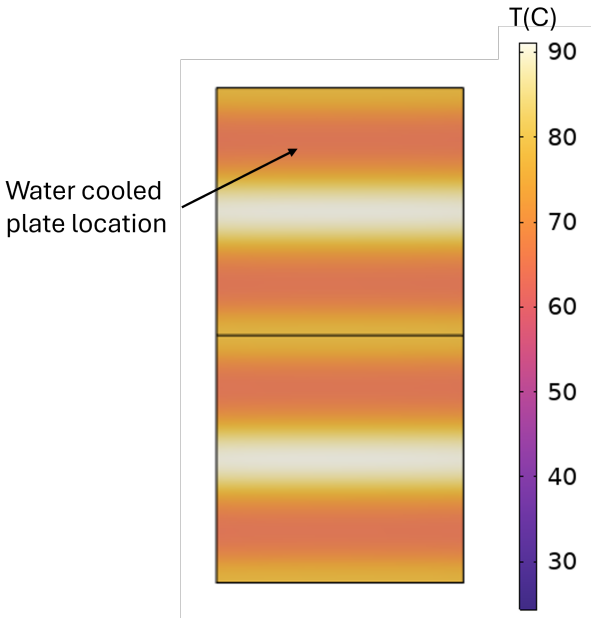

Figure 6: Thermal model predicted temperature distribution of the water cooled beam dump.

discharge voltage was fixed to 300 V, and we varied the discharge current to hit the target power. Figure 7 shows the discharge power as a function fo time for the 18 kW ramp.

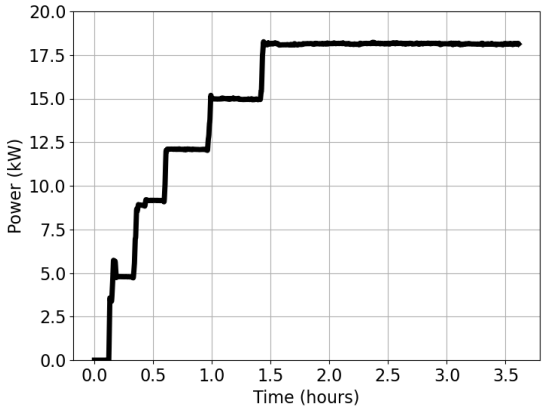

Figure 7: Thruster discharge power as a function of time for the extended duration test.

4 Facility Thermal Model

To aid our understanding of pump heating mechanisms, we built a 3D, steady-state thermal model of LVTF in COMSOL. The thermal model self-consistently solves for radiative, convective, and conductive heat loads from the 5 nude cryosails, 13 shrouded TM1200i's, the small water cooled beam dump, the standard beam dump, the chamber floor, and an example thruster. The main input heat load to the model is from the beam of the thruster, which we project downstream onto facility surfaces. We use the full facility model to primarily understand how radiative loading from the facility impacts

cryopump warming. A cutaway view of the predicted temperature distribution from this model is shown in fig. 8.

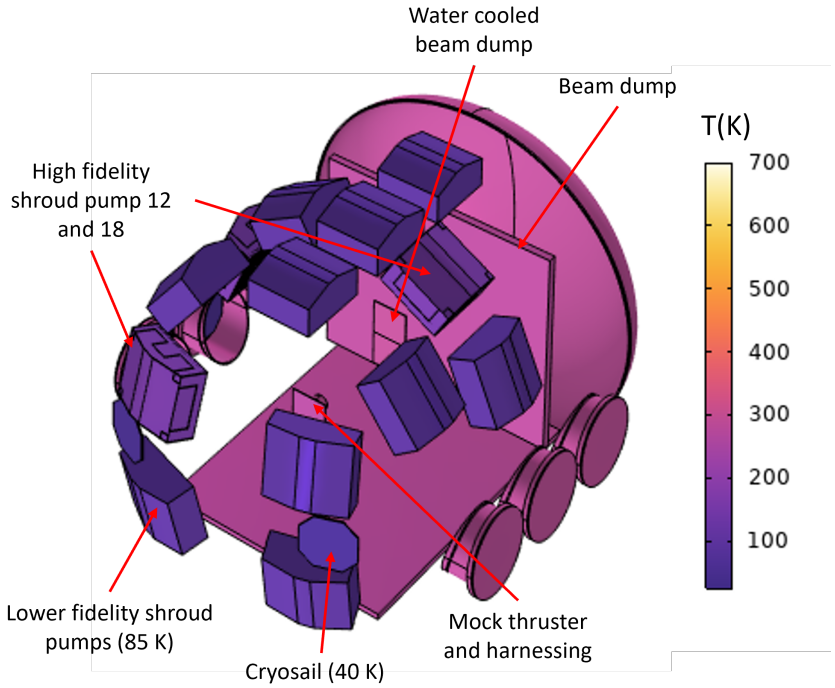

Figure 8: Thermal model of LVTF at the University of Michigan.

As part of the the facility model, we developed a sub-model of the shrouded TM1200i pump used in LVTF. Figure 9 shows the predicted temperature distribution of the TM1200i pump and a cutaway of the internal cold head.

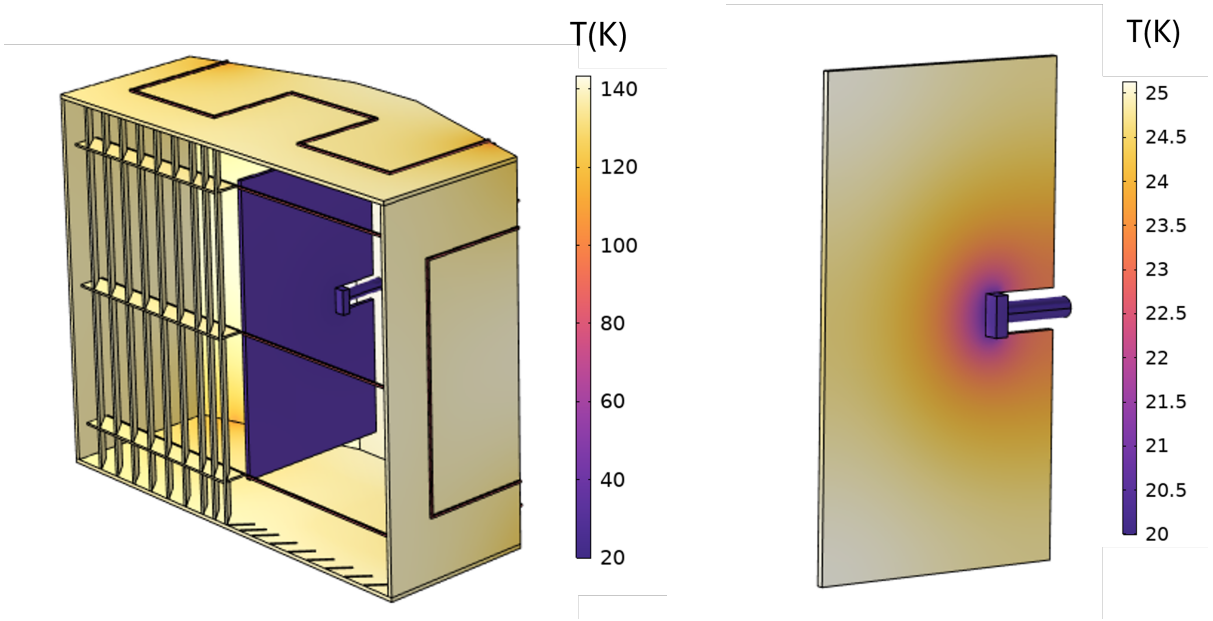

(a) (b)

Figure 9: Thermal simulations of a) the shrouded TM1200i cryopump and b) the internal cold head.

While we do not have access to the manufacture's CAD, we approximate the geometry

with detailed measurements and datasheet drawings. As a result, we expect there to be some discrepancies between the experimentally measured and modeled pump thermal response.

Per the manufacture, the shroud and the finned part of the cold head are made of aluminum, while the cryocooler cold head (small feature in fig. 9b) is made of copper. We assume the cold head is at a constant 20 K and is in perfect contact to the aluminum fin. Per the discussion in sec. 2, the shroud fins and internal structure have a high emissivity coating e_{coat} to prevent radiative reflections into the cold head. We did not have the manufacturer coating specifications available for this work, so we approximate its parameters from literature data. One common high emissivity coating used by NASA at cryogenic temperatures is Acktar Fractal Black. Detailed measurements of this coating indicate that at LN_2 shroud temperatures (77-125 K), the emissivity is ∼0.85 [16]. For the purposes of this analysis, we assume the coating of the TM1200i cryopumps is similar, and take $e_{coat} = 0.85$.

To provide cooling to the shroud, we model the LN_2 lines as solid pieces of aluminum with a 12.7 mm square cross section. We assume these lines are isothermal at T_{LN_2}, and that the LN_2 has a convective heat transfer coefficient of h_{LN_2}. We expect the LN_2 to be in two phase flow through the shroud, leading to higher temperatures than 77 K. To estimate T_{LN_2} and h_{LN_2} we measured select LN_2 shroud temperatures. The LN_2 shroud temperature sensor is located on the back of the pump, near where the cold head enters. These LN_2 measurements are shown in tab. 2. Unfortunately, we did not have this measurement available continuously during the test campaign.

Pump	7	8	10	12	13	17	18
T(K)	130	140	137	127	123	125	135

Table 2: Measurement of select LN_2 shroud temperatures in LVTF.

Table 2 demonstrates that the measured shroud temperatures are significantly higher than typical liquid nitrogen temperature of 77 K. The two primary drivers of this discrepancy are the location of the measurement, which has a large view factor to a warm ∼ 280 K wall, and the convective contact conductance of the liquid nitrogen. To calibrate our model with these measurements, we plot in fig. 10 the thermal model estimated shroud temperature (at the same location as the measurement) as a function of both T_{LN_2} and h_{LN_2}.

Fig. 10 shows that there is no unique combination of T_{LN_2} and h_{LN_2} that captures the average measured shroud temperature. Detailed studies of two phase LN_2 flow estimate the convective heat transfer coefficient to be ∼ 200 to 300 $W/m^2/K$ and trend down with mass flux [17]. For the purposes of this analysis, where our LN_2 mass flux may be reduced, we take the lower end of this range ∼ 200 $W/m^2/K$ as our estimate for h_{LN_2}. Correspondingly, to match the measured shroud temp, fig.10 indicates T_{LN_2} is ∼ $85K$. Here, we summarize the key assumptions/inputs of the full facility model.

- We only utilize a high fidelity model of the shrouded pump (fig. 9) in the locations of P18 and P12. The rest of the shrouded pumps are reduced fidelity isothermal "blocks" at $T = 85K$. While ideally we would model the full geometry of every TM1200i, this is computationally expensive and likely not required to identify key trends in the results.

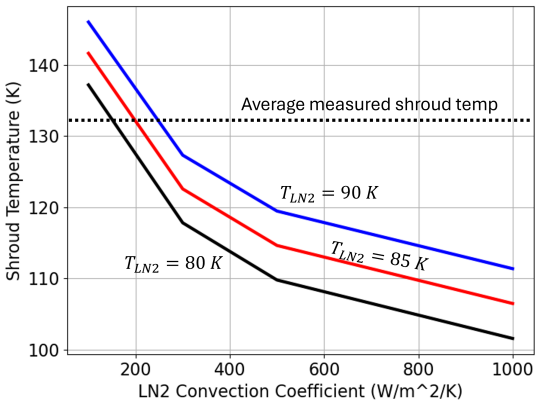

Figure 10: Thermal model predicted LN_2 shroud temperature as a function of the LN_2 temperature and convection coefficient.

- We assume all of the the thruster beam power hits either the standard or water cooled beam dump. In reality we do expect some of the thruster beam to directly hit LN_2 shrouds. We estimate the effect of beam impingement utilizing the high fidelity model of the TM1200i pump in sec. 5.3.
- The thruster beam power is $\sim$ 66 % of the discharge power [6]. We utilize the calibrated water cooled beam dump analysis to estimate the fraction of this beam power incident on the water cooled beam dump P_{WCBD}, with the rest on the standard beam dump P_{BD}. We neglect any angular distribution of beam power typically seen in Faraday traces [6] and assign the power uniformly across each beam dump.
- The outside of the chamber is convectively cooled by air at 20 C with a convective heat transfer coefficient h_{air} of 5 $W/m^2/K$. The value for the heat transfer coefficient was tuned to match the observed wall temperature with no load of $T_{wall} \approx 5$ C.

5 Moderate Power Facility Response

In this section, we overview the key results. We first present data for the water cooled beam dump, followed by the pump temperature response. We then use the observed pump thermal response and a facility thermal model to analyze the various cryopump heating mechanisms.

5.1 Water Cooled Beam Dump Results

As outlined in sec. 3.1, we implemented a prototype water cooled beam dump to assess its effectiveness at extracting thruster beam power. The more power we can efficiently extract into the water, the less thermal loading there will be on the facility and cryopumps. When designing the WCBD, our two main unknown parameters were the fraction of beam power hitting the plate η_{plate}, and the contact conductance of the graphite to the aluminum cold plates $h_{contact}$. The contact conductance ultimately controls how efficiently the WCBD extracts incident beam power (eq. 6). Using strategically positioned thermocouples on the WCBD (fig. 5), we directly measure the plate temperature and

power extracted from the water. With this data, we calibrate our two free model parameters to be $\eta_{plate} = 0.5$ and, $h_{contact} = 300$ W/m^2/K. Figure 11 shows the water power and plate temperature predictions for experimental data and calibrated thermal model.

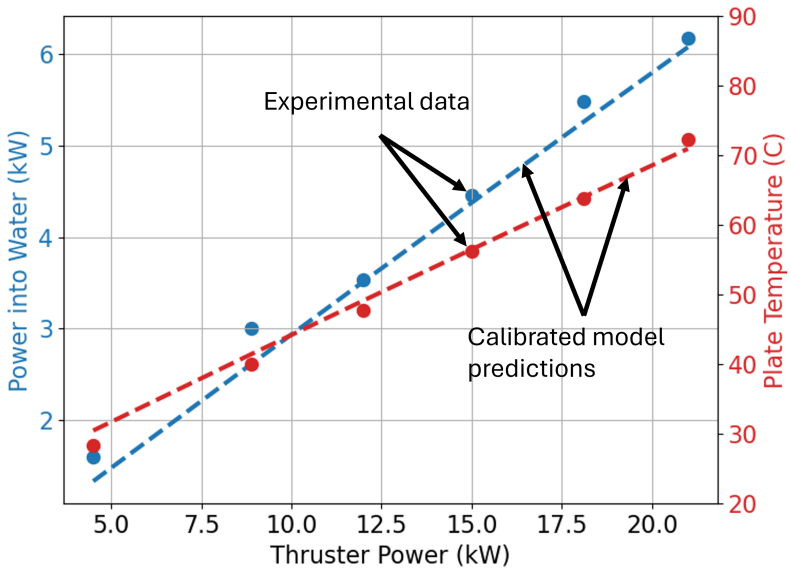

Figure 11: Experimentally measured and calibrated model predictions for extracted water power and plate temperature of the water cooled beam dump. Calibrated model parameters are $\eta_{plate} = 0.5$ and $h_{contact} = 300$ W/m^2/K.

As seen in figure 11, the calibrated model agrees well with the experimental data. With the calibrated model and eq. 6 we estimate the system efficiency, $\eta_{WCBD} = P_{water}/P_{plate}$, at 18 kW to be 88 %. The additional $\sim$ 12% is rejected primarily via radiation. The high system efficiency, and large fraction of beam subtended η_{plate}, are both indications that using a water cooled beam dump is an effective way to reduce facility thermal lading. Table 3 summarizes the calibrated parameters and system efficiency.

Parameter	Variable	Value
Aluminum to graphite contact conductance	$h_{contact}$	300 W/m^2/K
Fraction of beam power into WCBD plates	η_{plate}	0.5
WCBD efficiency at 18 kW	η_{WCBD}	88 %

Table 3: Water cooled beam dump model parameters and calculated efficiency.

5.2 Pump Response Results

In figure 12 we plot the cryopump cold head temperatures, normalized thruster power, and normalized pumping speed as a function of time for the 18 kW thruster ramp. The water cooled beam dump is installed and active during the entire thruster ramp. We note that since discharge voltage was fixed, the power/discharge current is proportional to the mass flow rate.

In fig. 12 we see that the initial cold head temperature of the shrouded pumps varies from 13-23 K. The nude cryosails, which are designed to operate warmer, have an initial

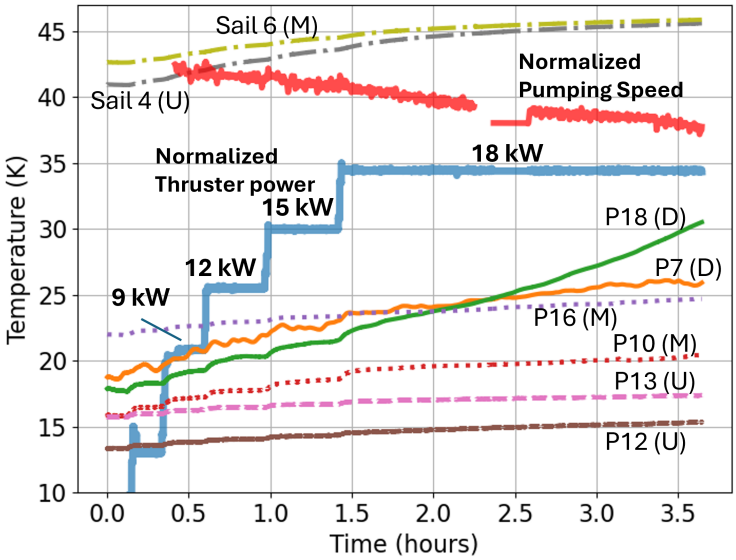

Figure 12: Facility cryopump temperatures, normalized thruster power, and normalized pumping speed as a function of time during the 18 kW thruster ramp. The tags "D", "M", and "U" refer to the pumps being downstream, mid-chamber (in plane), or upstream of the thruster. Pumps 9,11, and 17 are not shown for clarity/redundancy.

temperature of $\sim$ 42 K. In general, all pump temperatures in fig. 12 increase with both time and power level. We see a small (<1 K), rapid (< 10 min) cold head warming each time we increase the thruster power level. When at a constant thruster power, the pumps typically exhibit a more gradual increase in temperature. Both the pump temperature and the rate of increase is correlated with pump location in the chamber. In general, the downstream (P7/P18) and mid chamber pumps (P10/P16/Sail 6) have warmer initial cold head temperatures than the upstream versions (P12/P13/Sail 4). For the shrouded TM1200i's, the downstream pumps exhibit larger heating rates than either the mid chamber, or upstream versions. The nude sail heating rate is similar for both pumps.

As shown in fig. 3, a higher pump temperature is an indication of enhanced thermal loading to the cold head. For the shrouded pumps, this reveals there is a position dependent cryopump heat load both when the thruster is off and as we ramp in power. Most notably, after 3.5 hours of operation we see there is a $>$ 15 K difference between downstream pump 18 and upstream pump 12. Assuming the cryocooler performance in fig. 3 remains linear at higher temperatures (25-30 K), this temperature difference is an approximate heat load discrepancy of 15 W. Per our discussion in sec. 2, the heat load is likely coming from a combination of propellant thermal energy, radiation from the facility, or direct beam impingement on the shroud. All of these heating mechanisms increase with thruster power, but in sec. 5.3, we systematically evaluate each mode to assess which is the leading cause of the disparate pump thermal response in fig. 12.

Ultimately, the higher pump temperature/thermal load results in a constant decrease in the overall facility pumping speed. One explanation for the reduction in pumping speed is that propellants with low saturation temperatures N_2, Ar, O_2 etc. could be evaporating from the cold head surfaces. The evaporation results in a higher effective facility mass flow rate that is not included in eq. 4, resulting in a lower pumping speed. Furthermore,

since the cold head is cooled in a single location, we saw in sec. 4 that there can be a temperature gradient not captured by the single point temperature measurements in fig 12. Therefore, evaporation from locations on the warmer shrouded pumps (16, 7, or 18), may be higher than the temperature measurements indicate. It is also possible that consistent krypton evaporation comes from the cryosails (4, 6), which have initial temperatures close to the saturation temperature of 45 K at $P_b = 1 \times 10^{-5}$ Torr. With time or increasing power level, fig. 12 indicates that quick-warming cryopumps like P18 may eventually completely shed their krypton gas. In the next section, we attempt to explain the heating mechanisms that drive the pump thermal response trends of fig. 12.

5.3 Cryopump Heating Analysis

In this section, we utilize the cryopump thermal data in conjunction with the facility thermal model to understand what heating mechanisms drive the observed pump temperatures. As discussed in sec. 2, the three main heat drivers we consider are from propellant energy, facility radiation, and the thruster beam impinging on the LN_2 shroud. Identifying the key loading mechanisms will inform strategic decisions on how to modify the facility. Specifically, we want to identify what heating mechanism drives each of the following:

- The location dependent pump temperature differences with no load (T= 0 min).
- The rapid jumps in pump temperature when changing flow rate and thruster power level.
- The general increase in pump temperature with time.

5.3.1 Location Dependent Initial Pump Temperatures

An interesting aspect of fig. 12 is that the shrouded cryopumps without the thruster operating have a wide variety of temperatures $\sim$ 6-8 K. The temperature variation is much wider than the 2-3 K spread LVTF pump temperatures reported in ref. [11]. One possibility is that overtime, the performance of the cryocooler and compressor has changed non-uniformly, leading to a different load vs temperature curve than seen in fig 3. While it is possible that some deviations in the cryocooler performance exist, this explanation alone does not resolve why pumps downstream of the thruster and some mid chamber pumps are warmer than their upstream counterparts.

Given that the cryocooler performance likely does not explain the spatially dependent initial pump temperature difference, it appears that under very similar ambient conditions, the cold heads are receiving different heat loads. As a result, it seems likely that the thermal parameters of the pumps vary across the facility. The two parameters to consider are the LN_2 temperature/convective heat transfer coefficient, and the shroud emissivity.

One potential suspect is that the temperature and convective heat transfer coefficient of the liquid nitrogen varies. However, if we look at the measured LN_2 shroud temperatures in tab. 2, we see there is no clear trend with location in the chamber. Furthermore, we see that the largest temperature difference in measured shroud temperatures is between pump 10 and pump 13, which have the same initial cold head temperature. As a result, we can largely rule out that differences in liquid nitrogen temperature or convective heat transfer coefficient are causing the initial pump temperature discrepancy.

Another thermal parameter of the pumps that could cause the initial pump temperature discrepancy is the surface emissivity. As discussed in sec. 2, the high emissivity coating on the shroud surfaces serves to absorb ambient radiation and prevents it from reflecting into the cold head. If the high emissivity coating on the downstream pumps has been preferentially eroded or deposited onto over time, this could lead to enhanced cold head radiative loading. As evidence of this process occurring, in fig. 13a we show a comparison between a new TM1200i cryopump and the current state of the pumps in LVTF. Additionally, in fig. 13b, we show the predicted cryopump radiative loading difference between pump 18 with and without the high emissivity coating. To estimate the radiative load, we utilize the facility thermal model introduced in sec. 4, assuming the thruster is off.

(a)

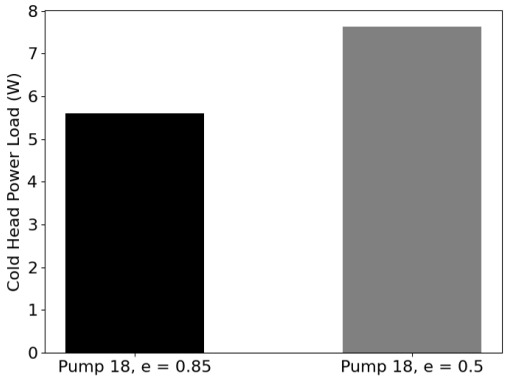

(b)

Figure 13

Figure 13a, clearly shows a drastic change in the pump surface over time. Analyzing the surface, we found that there is deposited layer from back sputtered material covering the high emissivity coating. The deposited material, which is a combination of steel, aluminum, and graphite, likely reduces the absorption of ambient radiation by the shroud. The layer of deposited material was thicker for downstream pumps, which have greater view factor to sputtered material, than their upstream counterparts.

In fig. 13a, we see that if the emissivity drops to 0.5 as a result of deposition onto shrouds, our thermal predicts greater than a 2 W difference from ambient thermal loading. It is possible the emissivity of the some pump surfaces is even lower than 0.5, resulting in thermal loading differences commensurate with the $\sim$ 6-8 W discrepancy seen in fig. 12. With evidence supported by both visual inspection and modeling, it is highly likely that a difference in pump emissivity is driving the initial temperature differences seen in fig. 12.

5.3.2 Rapid Changes in Pump Temperatures

Notably, fig. 12 shows that there is a rapid cold head temperature increase when the thruster flow rate and power change. Given the high thermal conductivity of the cold head, a rapid change in temperature is indicative of a rapid change in power loading. To better illustrate this effect, in fig. 14a we isolate the change in temperature of pumps 18 and 12 to thruster hot flow. For comparison, in fig. 14b we plot the change in temperature of the same pumps in response to cold flow. We perform the cold flow test by metering flow through the anode without the discharge.

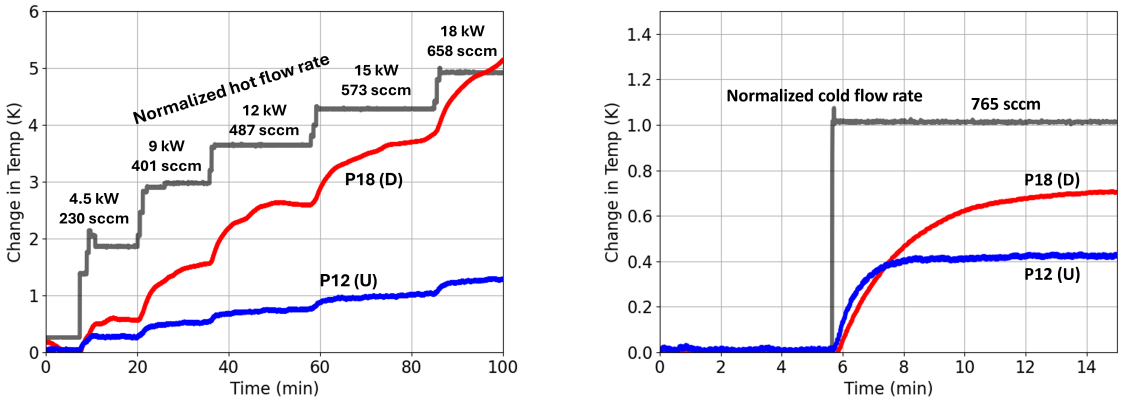

(a) (b)

Figure 14: Pump 12 and 18 temperature response to a) hot flow and b) cold flow.

For both the cold and hot flow data, we see a rapid response in the pump temperatures when changing flow rate and thruster power. For the hot flow, both propellant loading and beam impingement likely contribute to the rapid temperature rise. The cold flow data is direct evidence that the fast thermal propellant velocities can quickly load the cold head. Since the LN_2 shroud has a high thermal conductivity and is backed by convective cooling, the direct beam impingement should also induce fast temperature changes. Figure 15 shows the thermal model estimated change in cold head power load as function of shroud power loading.

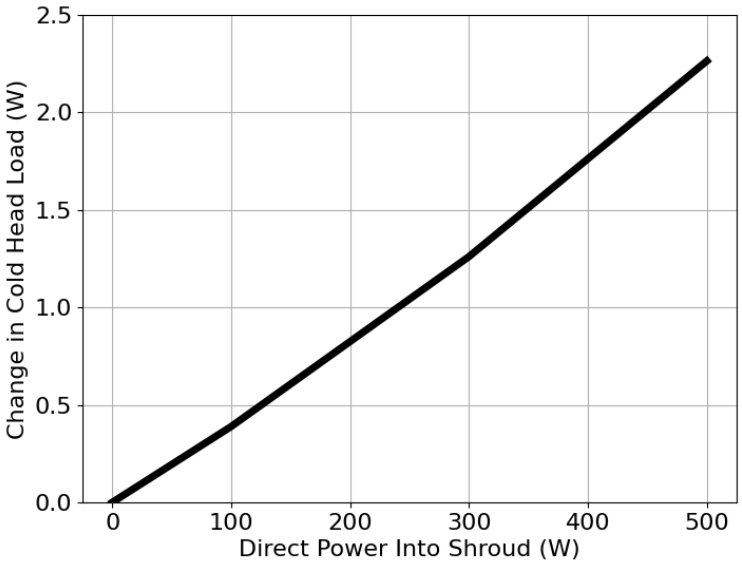

Figure 15: Cold head power loading as a function of beam power incident on the shroud.

We first analyze the cold flow temperature response shown in fig. 14b to aid in understanding the relative contribution of propellant loading to hot flow in fig. 14a. Per fig. 3, we again assume that a 1 K change in temperature is equal to an additional 1 W of cold head load. With this metric, we see that pump 18 and 12 have $\sim$ 0.75 W and 0.4 W of heating in response to 765 sccm of cold flow. Assuming that all gas thermalizes

with the LN_2 shroud at 100 K, we use eq. 1 to estimate that $\sim$ 85 and 45 sccm of gas flow is hitting pumps 18 and 12 respectively. This indicates that P18 receives $\sim$ 11 % of the total flow, while P12 receives $\sim$ 6 %. Consistent with these results, qualitatively, we expected pump 18 to receive more flow due to its location in the chamber.

As expected, fig. 14a indicates that both pump 18 and pump 12 experience a larger thermal response to hot flow than cold flow. Even with less total propellant flow rate (85 sccm less), the pumps exhibit an additional $\sim$ 4 and 1 W increase in heating for the hot flow case. Given the only difference between the hot and cold flow is the beam energy, the additional loading must be driven by a combination of beam impingement and propellant thermal/bulk energy. The larger relative increase for pump 18 compared to 12 indicates a large fraction of pump 18 load is from beam impingement. Furthermore, direct beam impingement could be sourcing high energy ions preferentially to downstream pumps, resulting in enhanced thermal loading.

To calculate the relative contribution of heating from the beam, we focus on the 9-18 kW power ramp in fig. 14a. In this ramp, there are there are three jumps in power of 3 kW and $\sim$ 85 sccm. The total power load for each 3 kW jump is $\sim$ 1 W for P18 and 0.2 W for P12. Assuming the fraction of the gas to each pump remains the same between hot flow and cold flow, each 85 sccm flow rate increase results propellant deposition heat loads of only 0.08 W to P18 (9.4 sccm) and .04 W to P12 (5.1 sccm). With the approximate propellant deposition load, we estimate that every 3 kW increase in power results in 0.9 W and 0.15 W of beam loading to P18 and P12. This indicates that the thruster beam power dominates the rapid increase in thermal loading seen in fig. 14a. Assuming the scaling remains the same to 100 kW, the beam loading could be as high as 30 W to P18. Given this large predicted load, we must take steps to mitigate direct ion collisions with shrouds/cold heads.

5.3.3 General Pump Temperature Increase

Lastly, we assess which of the cryopump heat sources could lead to the general increase in pump temperature with time observed in fig. 12. The heating rate is most pronounced in downstream pump 18, but even colder pumps like P12 still show an upward trend. As discussed in sec. 5.3.2, we expect the high conductivity copper cold head to respond rapidly to any changes in thermal loading. Therefore, the heating mechanism driving the long-term pump temperature changes must also be increasing on longer timescales.

Given the timescales, only thermal radiation from the thruster and facility, which increase gradually with time, could be the cause of the general increase in pump temperature. Indeed, in fig. 16a we see that the normalized thruster temperature continually increases throughout the length of the test. This indicates an increasing radiative load with time, which is observed in fig. 12 as an increase in pump temperatures. In contrast, propellant loading and beam power impinging on the shroud tend to cause rapid thermal loading, as discussed in sec. 5.3.2. While the thermal models developed in this work are steady state, in fig. 16b we simulate the effect of an increasing radiative load with time by plotting the predicted cold head heat load as a function of ambient temperature.

As expected, fig. 16b illustrates that the thermal load to the cryopump cold head increases with ambient temperature. Notably, due the quartic scaling of radiative heat transfer, the thermal load is non-linear. This non-linear increase in thermal load is qualitatively similar to the heating we see in downstream pump 18 in fig. 12. This indicates P18 receives a proportionally larger radiative load than the other shrouded chamber pumps. This could be due to a larger view factor to hot facility radiation in

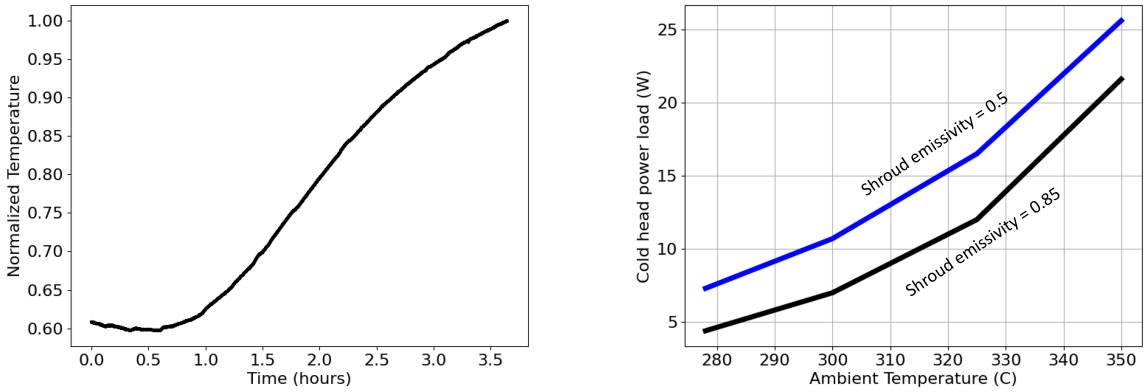

(a) (b)

Figure 16: a) Normalized thruster temperature as a function of time. b) Cold head thermal loading with increasing ambient temperature.

combination with a more reflective shroud (sec. 5.3.1) than other pumps.

6 Facility Modifications for 100 kW Testing

Armed with our understanding of the pump heating mechanisms in LVTF, we propose three key facility changes to test at the 100 kW level for extended durations. The main modifications are as follows:

- Restore the high emissivity coating on pump surfaces.
- Move the location of the thruster to avoid direct beam impingement on pump surfaces.
- Design and build a larger water cooled beam dump to efficiently extract power at 100 kW.

As illustrated in fig. 13a, we see that the high emissivity coating on the shroud has changed significantly since initial install. Analysis of the pump shroud revealed that this was primarily due to back sputtered material (graphite, steel, aluminum). The net effect of this change is a lowering of the surface emissivity, which increases the amount of reflected radiated power to the internal cold head. To remedy this, we will clean each of the LN_2 shrouds in LVTF. After restoring the high emissivity coating, the pump temperatures should return to similar temperatures ($\sim$15 K) under ambient load as was seen in ref. [11]. This modification will make the cryopumps more resilient to ambient thermal loading, which is key for high powered EP testing.

The next facility change is to move the position of the thruster in the chamber downstream to avoid direct beam impingement on the pumps. In fig. 17, we show the approximate new location of the thruster. Per our discussion in sec. 5.3, high energy thruster ions, whether from the main beam or charge exchange collisions, appear to be impacting pump surfaces. These ions deposit energy into the shroud and carry bulk velocity into the internal cold head. Indeed, we estimated in sec. 5.3.2 for P18 that a change in 3 kW of thruster power for the H9 at 300 V approximately results in an additional 0.8-0.9 W

of beam impact induced heating. Extrapolating these estimates to 100 kW, the thermal load from beam impingement alone on pump 18 could be as high as 30 W. When combined with facility radiation and propellant deposition, the cold head temperature at 100 kW could be >50 K– well beyond krypton saturation.

To avoid this issue, we will move the thruster to be approximately in plane with the downstream pumps (fig. 17). One possible downside of this change is an increase in thruster near field background pressure due to the shifted pump location. While a higher background pressure is less representative of on orbit testing, it is potentially a necessary tradeoff, based on the geometry of LVTF, to test at the 100 kW level.

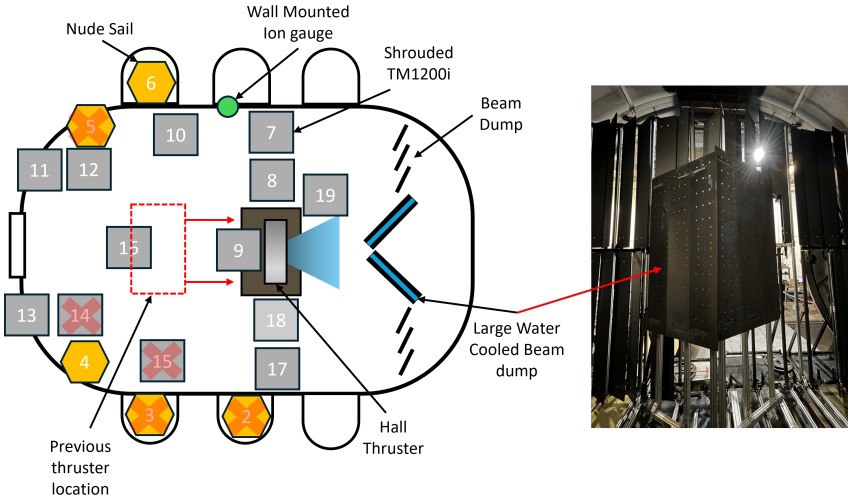

Figure 17: Facility diagram of LVTF with the downstream shifted thruster position to avoid beam impingement on pumps. Also pictured is the large water cooled beam dump designed for 100 kW testing.

The last change, as seen in fig. 17, is to scale the small water cooled beam dump to a larger design. While the small WCBD performed well (we experimentally found $\eta_{WCBD} \approx 88\%$), at the moderate operating powers of the initial test campaign, the performance drops to $< 70\%$ at the 100 kW level. The drop in performance is driven by the system thermal resistance to conduction, causing the graphite plate temperature and radiative load to rise quickly. If we build a larger design with more cold plates, the overall resistance to conduction is lower, increasing performance. Furthermore, a larger design allows us to subtend more of the thruster beam without having to move the WCBD closer to the thruster. Moving the small water cooled beam dump closer to the device could cause a significant increase neutral pressure and carbon back sputter onto the thruster.

Ultimately, we designed the size/position of the larger water cooled beam dump to subtend $> 75\%$ of the thruster beam. The required size was estimated using the same techniques as described in sec. 3.1. Thruster Faraday traces and eq. 5, estimate that as much as 85% of the beam power is subtended. We simulate the larger water cooled design in the LVTF thermal model to assess its effectiveness at reducing radiative loading to the cryopump cold head surface. For this initial model, we assume that 75 % of the beam power is incident on the water cooled beam dump. In fig. 18, we compare facility radiative loading to cold head 18 as a function of thruster power for three cases: the bare facility, the small WCBD, and the large WCBD. In all cases, we assume the the high emissivity of shroud surfaces has been restored.

As expected, in fig. 18 we see an increase in radiative loading to cold head 18 with

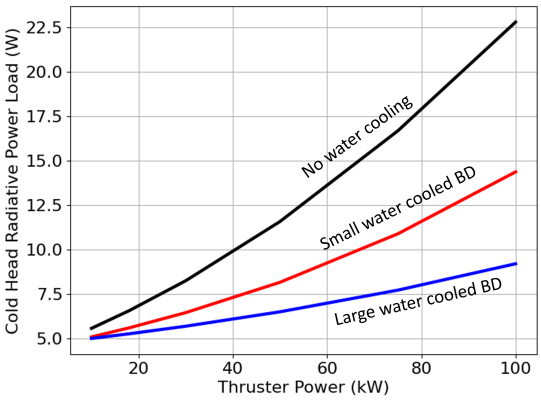

Figure 18: Radiative thermal loading to the cold head of pump 18 as a function of thruster power and facility configuration.

thruster power. We also see that there is a significant decrease in thermal loading to the pump with the large WCBD compared to the other cases. Indeed, at 100 kW, the large WCBD reduces the thermal load by over 5 W compared the the small version. To illustrate the major impact these three facility modifications will have on testing at 100 kW in LVTF, we plot in fig. 19 the predicted current cold head power loading of pump 18 to that after the LVTF changes.

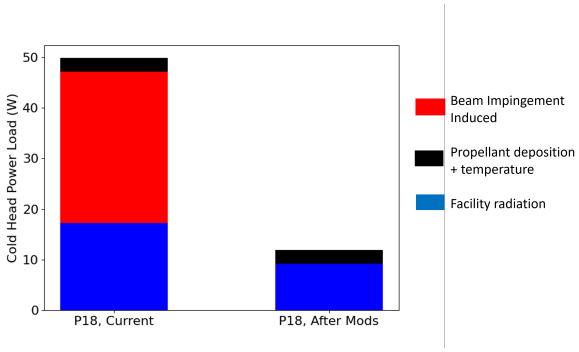

Figure 19: Pump 18 predicted thermal loading before and after LVTF facility modifications.

To generate our estimate of beam impingement for the current facility, we extrapolate the observed results in sec. 5.3.2 and assume a $\sim$ 30 W increase in power load at 100 kW (based on 0.9 W delta for a 3 kW thruster change.) After moving the thruster, we assume the beam does not impinge on the surfaces. We utilize the facility thermal model to estimate the predicted radiative loads in each case. For propellant deposition, we assume the flow rate at 300 V, 100 kW is $\sim$ 3000 sccm (50 % efficiency at $I_{sp} = 2500s$ [6]), and that 10 % (see sec. 5.3.2) of the propellant deposits onto cryopump 18 at a temperature of 100 K.

Under these assumptions, we see a that there is a $\sim$ 38 W difference in the cold head loading as a result of the new modifications. This is in large part driven by moving the thruster location and avoiding direct beam impingement. There is also a change of $\sim$ 8 W in facility radiative loading to the pump, which is the result of pump emissivity restoration and the large water cooled beam dump. Overall, the total predicted thermal load to pump 18 after modification is 12 W. Based on the cryocooler response to thermal

load (fig. 3), this will keep the cold head temperature well below the 41 K limit to pump krypton at partial pressures $< 1 \times 10^{-6}$ Torr. Therefore, with these facility changes, we are confident in our ability to test for long durations in LVTF at 100 kW.

7 Conclusion

High powered electric propulsion devices induce large thermal stress on the cryopumps in ground test chambers. Maintaining low cryopump surface temperature is essential to rapidly evacuate common gaseous electric propulsion propellants like xenon, krypton, and argon. The goal of this work is to understand the relative sources of heat loading to the cryopumps in the Large Vacuum Test Facility at the University of Michigan so we can make key facility modifications that allow for long duration testing at 100 kW. To understand the loads, we first directly measured the pump temperatures in response to 18 kW Hall thruster operation. In parallel, we determined that a small water cooled beam dump could efficiently extract thruster beam power and reduce cryopump loading from the facility. Using a series of calibrated thermal models in conjunction with the experimental data, we determined that differences in surface emissivities between downstream and upstream pumps contributes to the thermal load discrepancies. The surface coating of downstream pumps was preferentially deposited onto, leading to enhanced cold head loading. We also found that direct thruster beam impingement on downstream pumps induced large thermal loads that would far exceed cryocooler capacity at the 100 kW scale. To test at the 100 kW scale, we proposed to restore the emissivity of pump surfaces, move the thruster downstream to avoid beam impingement, and build a large water cooled beam dump to extract beam power. Predicted pump thermal loads after these changes suggests that in the future we will be able to test at 100 kW in LVTF without risk of cryopump overheating.

References

[1] S. Bays, D. Choe, D. Tucker, A. Wagner, D. Burns, R. O'Brien, and P. Talbot, "Mars Transportation Assessment Study," tech. rep., NASA, 2023.

[2] E. N. A. o. Sciences, Medicine, and other, *Space Nuclear Propulsion for Human Mars Exploration*. 2021.

[3] S. R. Oleson, L. M. Burke, L. S. Mason, E. R. Turnbull, S. McCarty, A. J. Colozza, J. E. Fittje, J. T. Yim, M. Smith, T. W. Packard, *et al.*, "Compass final report: Nuclear electric propulsion (NEP)-chemical vehicle 1.2," tech. rep., NASA, 2021.

[4] S. W. Shark, S. J. Hall, B. Jorns, R. R. Hofer, and D. M. Goebel, "High power demonstration of a 100 kW nested Hall thruster system," *AIAA Propulsion and Energy 2019 Forum*, 2019, p. 3809.

[5] L. L. Su, P. J. Roberts, T. Gill, W. Hurley, T. A. Marks, C. L. Sercel, M. Allen, C. B. Whittaker, M. Byrne, Z. Brown, *et al.*, "Operation and performance of a magnetically shielded Hall thruster at ultrahigh current densities on xenon and krypton," *AIAA Scitech 2023 Forum*, 2023, p. 0842.

[6] L. L. Su, P. J. Roberts, T. M. Gill, W. J. Hurley, T. A. Marks, C. L. Sercel, M. G. Allen, C. B. Whittaker, E. Viges, and B. A. Jorns, "High-current density performance

of a magnetically shielded hall thruster," *Journal of Propulsion and Power*, 2024, pp. 1–18.

[7] A. Ferreira and L. Lobo, "The sublimation of argon, krypton, and xenon," *The Journal of Chemical Thermodynamics*, Vol. 40, No. 12, 2008, pp. 1621–1626.

[8] N. I. o. Standards and Technology, *NIST Chemistry WebBook: NIST Standard Reference Database Number 69*. Gaithersburg, MD: NIST, 2000. Accessed: [4/10/24].

[9] A. Neumann and M. Brchnelova, "Modelling of Cryopumps for Space Electric Propulsion Usage," *Aerospace*, Vol. 11, No. 3, 2024, p. 177.

[10] F. P. Incropera, D. P. DeWitt, T. L. Bergman, A. S. Lavine, *et al.*, *Fundamentals of heat and mass transfer*, Vol. 1072. New York John Wiley & Sons, Inc., 1990.

[11] E. A. Viges, B. A. Jorns, A. D. Gallimore, and J. Sheehan, "University of Michigan's upgraded large vacuum test facility," *36th International Electric Propulsion Conference*, 2019, pp. 1–18.

[12] P. Technologies, "CGR-511 Cryocooler," `https://www.phpk.com/cryopumps/cryocoolers/`, n.d. Accessed: 2025-09-11.

[13] K. D. Diamant, T. J. Curtiss, R. Spektor, E. J. Beiting, V. Hruby, B. Pote, J. Kolencik, and S. Paintal, "Performance and plume characterization of the BHT-1500 Hall thruster," *Joint Conference of 30 th International Symposium on Space Technology and Science 34th International Electric Propulsion Conference and 6th Nano-satellite Symposium (4–10 July 2015, Hyogo-Kobe, Japan). IEPC-2015-69*, 2015.

[14] M. Cooper, B. Mikic, and M. M. Yovanovich, "Thermal contact conductance," *International Journal of heat and mass transfer*, Vol. 12, No. 3, 1969, pp. 279–300.

[15] R. R. Hofer, S. E. Cusson, R. B. Lobbia, and A. D. Gallimore, "The H9 magnetically shielded Hall thruster," *35th International Electric Propulsion Conference*, Electric Rocket Propulsion Society, 2017, pp. 2017–232.

[16] D. Katsir, T. Králík, and J. Frolec, "Emissivity of black coatings from ambient to cryogenic temperatures: how spectrally flat black coatings can enhance performance of space systems," 2023.

[17] S. R. Darr and J. W. Hartwig, "Two-phase convection heat transfer correlations for liquid hydrogen pipe chilldown," *Cryogenics*, Vol. 105, 2020, p. 102999.